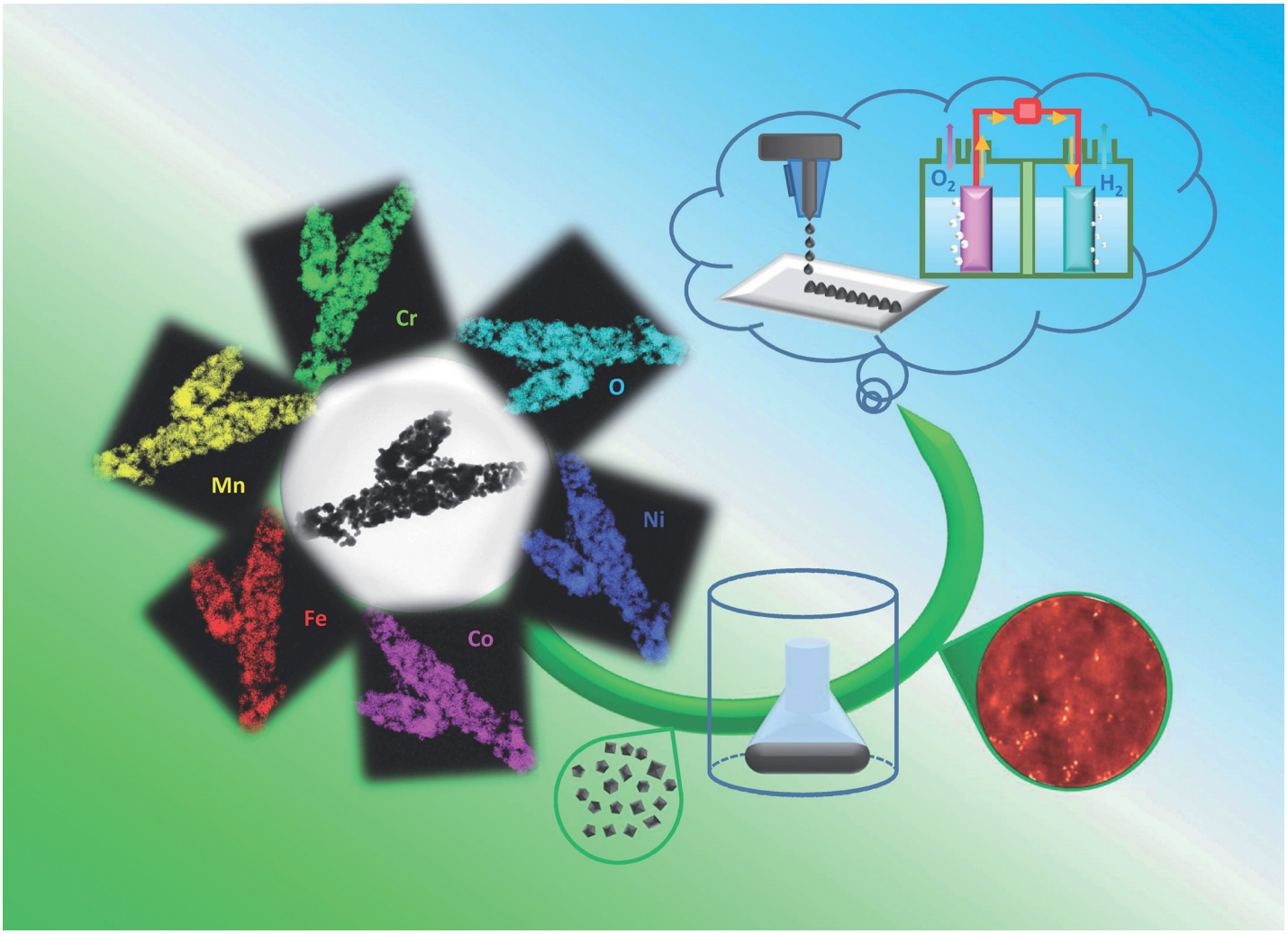

Showcasing research from Professor Saveria Santangelo's laboratory, DICEAM, Mediterranean University, Reggio Calabria, Italy.

Evaluation of electrospun spinel-type high-entropy $(Cr_{0.2}Mn_{0.2}Fe_{0.2}Co_{0.2}Ni_{0.2})_3O_4$, $(Cr_{0.2}Mn_{0.2}Fe_{0.2}Co_{0.2}Zn_{0.2})_3O_4$ and $(Cr_{0.2}Mn_{0.2}Fe_{0.2}Ni_{0.2}Zn_{0.2})_3O_4$ oxide nanofibers as electrocatalysts for oxygen evolution in alkaline medium

Electrospun spinel-type (Cr,Mn,Fe,Co,Ni), (Cr,Mn,Fe,Co,Zn) and (Cr,Mn,Fe,Ni,Zn) high-entropy oxide nanofibers are evaluated as electrocatalysts for oxygen evolution in alkaline medium. Their electrochemical performance depends on the metal combination and is understood in terms of occupation of octahedral sites by redox-active centers and oxygen vacancy surface defects. Thanks to the possibility of easily separating the small-sized grains that make up the fibres from each other, these materials have great potential as inkjet printable electrocatalysts.

As featured in:

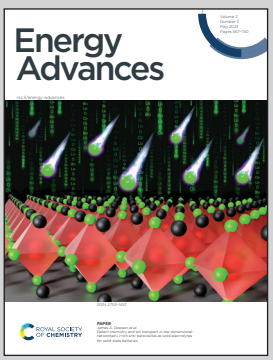

See Ben Breitung, Saveria Santangelo *et al.*, *Energy Adv.*, 2023, **2**, 667.

ROYAL SOCIETY OF CHEMISTRY

rsc.li/energy-advances

Registered charity number: 207890

Energy Advances

ROYAL SOCIETY OF CHEMISTRY

PAPER

View Article Online
View Journal | View Issue

Cite this: *Energy Adv.*, 2023, 2, 667

Evaluation of electrospun spinel-type high-entropy $(Cr_{0.2}Mn_{0.2}Fe_{0.2}Co_{0.2}Ni_{0.2})_3O_4$, $(Cr_{0.2}Mn_{0.2}Fe_{0.2}Co_{0.2}Zn_{0.2})_3O_4$ and $(Cr_{0.2}Mn_{0.2}Fe_{0.2}Ni_{0.2}Zn_{0.2})_3O_4$ oxide nanofibers as electrocatalysts for oxygen evolution in alkaline medium†

Claudia Triolo, [ab] Simon Schweidler, [c] Ling Lin, [c] Gioele Pagot, [bd] Vito Di Noto, [bd] Ben Breitung *[c] and Saveria Santangelo *[ab]

Received 6th February 2023,
Accepted 2nd April 2023

DOI: 10.1039/d3ya00062a

rsc.li/energy-advances

Electrochemical water splitting is a promising sustainable-energy technology, but the slow kinetics of the oxygen evolution reaction represents a limitation for its broad market penetration. Spinel-structured transition metal (TM) oxides have shown great potential as a sustainable alternative to precious metal-based electrocatalysts. High-entropy oxides (HEOs) with multiple TM-cation sites lend themselves to engineering of the octahedral redox-active centres to enhance the catalyst reactivity. This work focuses on the preparation of electrospun spinel-type HEO nanofibers (NFs), based on equimolar (Cr,Mn,Fe,Co,Ni), (Cr,Mn,Fe,Co,Zn) and (Cr,Mn,Fe,Ni,Zn) combinations, and their evaluation as electrocatalysts in alkaline medium together with (Cr,Mn,Fe,Co,Ni) HEO nanoparticles (NPs) prepared *via* the sol–gel method. $(Cr_{0.2}Mn_{0.2}Fe_{0.2}Co_{0.2}Ni_{0.2})_3O_4$ NFs and NPs (Tafel slopes: 49.1 and 51.3 mV dec^{-1}, respectively) outperform both $(Cr_{0.2}Mn_{0.2}Fe_{0.2}Co_{0.2}Zn_{0.2})_3O_4$ and $(Cr_{0.2}Mn_{0.2}Fe_{0.2}Ni_{0.2}Zn_{0.2})_3O_4$ NFs (62.5 and 59.6 mV dec^{-1}, respectively) and IrO_2 reference electrocatalyst (52.9 mV dec^{-1}). The higher concentration of oxygen vacancies on their surface and the higher occupation of octahedral sites by redox-active Co^{2+} and Ni^{2+} centres are responsible for their behaviour. The present electrospun HEO NFs have great potential as ink-jet printable electrocatalysts.

Introduction

To combat climate change induced by anthropogenic action, it is urgent to reduce the use of fossil fuels more and more and to progressively replace them with environmentally friendly renewable sources with low carbon emissions, such as solar and wind energies. With its high energy density, hydrogen is an ideal alternative energy source to achieve the goal of carbon neutrality and its production through water splitting (WS) is increasing.[1–3] The process involves the hydrogen evolution reaction (HER) on the cathode and the oxygen evolution reaction (OER) on the anode of the electrolyser.[4–7] The former reaction proceeds through the transfer of two electrons, while the latter involves four electrons and multiple intermediates. As a result, OER is kinetically slower and represents the speed-limiting step of the WS process. Therefore, to improve the efficiency of WS it is essential to reduce the kinetic limitation of the OER. Several strategies have been implemented for this purpose.[8,9]

Currently, noble metal-based electrocatalysts, such as IrO_2 and RuO_2,[7–11] are considered the state-of-the-art electrocatalysts for reducing overpotential and increasing the rate of OER. However, their scarcity and high cost drastically limit the large-scale application. This calls for the development of more sustainable, high performance electrocatalysts. Transition metals (TMs) and particularly spinel-structured TM oxides have been extensively evaluated as alternative OER electrocatalysts.[12–15] Their outstanding catalytic performance, large abundance, low

[a] *Dipartimento di Ingegneria Civile, dell'Energia, dell'Ambiente e dei Materiali (DICEAM), Università "Mediterranea", Via Zehender s.n.c., Loc. Feo di Vito, 89122 Reggio Calabria, Italy. E-mail: saveria.santangelo@unirc.it*
[b] *National Reference Center for Electrochemical Energy Storage (GISEL), Consorzio Interuniversitario Nazionale per la Scienza e Tecnologia dei Materiali (INSTM), 50121 Firenze, Italy*
[c] *Institute of Nanotechnology, Karlsruhe Institute of Technology (KIT), Hermann-von-Helmholtz-Platz 1, 76344 Eggenstein-Leopoldshafen, Germany. E-mail: ben.breitung@kit.edu*
[d] *Section of Chemistry for the Technology (ChemTech), Department of Industrial Engineering, University of Padova, Via Marzolo 9, 35131 Padova (PD), Italy*

† Electronic supplementary information (ESI) available. See DOI: https://doi.org/10.1039/d3ya00062a

cost and stability make them very attractive anode materials for the WS process, particularly in alkaline medium.[16]

The spinel structure is very open to accommodate the migration of cations.[17] The O^{2-} anions are arranged in a cubic close packed sublattice and each of them is shared amongst its four nearest TM cations.[18] The TM cations occupy a quarter of the 96 sites available in the $(M_{1-\lambda}^{2+}M_{\lambda}^{3+})_{8a}(M_{\lambda}^{2+}M_{2-\lambda}^{3+})_{16d}O_4$ spinel lattice;[19,20] 64 of them have tetrahedral geometry (8a sites, in the Wyckoff notation, four O-coordinated, Fig. S1a, ESI†) and the remaining 32 ones have octahedral geometry (16d sites, six O-coordinated, Fig. S1b, ESI†).[18,21] λ is the so-called inversion degree, *i.e.* the fraction of M^{3+} cations in the 8a sublattice; it varies between 0 for the ''normal spinel'' structure, with 1/8 of the available tetrahedral sites occupied by M^{2+} cations and M^{3+} cations occupying 1/2 of the available octahedral sites, and 1 for the ''inverse spinel'' structure, with all M^{2+} cations located at 8 octahedral sites and M^{3+} cations occupying 8 octahedral and 8 tetrahedral sites.[20–22] The inversion degree is sensitive to the synthesis conditions, as well as to the combination and nature of TM cations. The higher the inversion degrees, the higher the bulk conductivity.[23,24] The TM cations located at the 8a and 16d sites exhibit different behaviour both in terms of chemisorption and electrocatalytic activity.[25] The $M^{3+}O_6$ octahedra possess higher degree of M–O covalence than the $M^{2+}O_4$ tetrahedra because of the higher electronic charge that O shares with TM.[17,26] The greater hybridisation between O 2p and TM 3d orbitals results in enhanced OER activity due to the facilitated electron transfer between the redox-active TM centre of the oxide and oxygen,[17] with the filling of the TM 3d orbitals split by the crystal field governing the binding strength of the OER intermediates. The concentration of the oxygen vacancies also matters,[17,25,27–35] as they favour the adsorption of oxygen intermediates,[17] thus enhancing the electrocatalytic performance.[27]

Based on the relationship existing between the cation distribution and the reactivity of the catalyst, many efforts have been made to enhance the octahedral redox-active TM centres in spinel-structured electrocatalysts by replacing tetrahedral cations with elements suitable for pushing the oxygen charge towards the octahedral ones.[17,25,26,36,37] Coordinately unsaturated metal octahedra MO_{6-x} on the surface, introduced by the transformation from tetrahedral to octahedral coordinated cation, are believed to be the active centres for the OER.[25]

In this scenery, high-entropy materials (HEMs) with multiple TM-cation sites exhibit great potential for application as electrocatalysts.[28,29,38,39] Among HEMs, high-entropy alloys (HEAs) have been broadly investigated as both HER and OER electrocatalysts.[40–46] Nguyen *et al.*[47] have reported outstanding OER performance for $La(CrMnFeCo_2Ni)O_3$ high entropy oxide (HEO) with perovskite structure. Sun *et al.*[48] have shown that $(Cr_{0.2}Mn_{0.2}Fe_{0.2}Co_{0.2}Ni_{0.2})_3O_4$ HEO powders exhibit excellent Li^+-storage capability and lower overpotential and Tafel slope than spinel-type moderate entropy (four-metal) oxides in WS. Additionally, a mesoporous $(Cr_{0.2}Mn_{0.2}Fe_{0.2}Co_{0.2}Ni_{0.2})_3O_4$ HEO thin film has been proven to outperform the dense film.[27] Stenzel *et al.*[49] have reported that spinel-structured five-TM HEOs give better overpotential and Tafel slope values than IrO_2, with $(Mg_{0.2}Cr_{0.2}Mn_{0.2}Fe_{0.2}Ni_{0.2})_3O_4$ HEO exhibiting the best performance (293 mV overpotential at 10 mA cm^{-2} and 46.5 mV dec^{-1} Tafel slope).

The design of non-noble metal based nanocatalysts with a large surface area and an easily tunable composition is of pivotal importance to overcome the limitations imposed by the sluggish kinetics and large overpotential. Electrospinning (ES) allows producing oxides in the form of nanofibers (NFs) on an industrial scale.[50–52] Thanks to their large surface area, high aspect ratio and hierarchical porosity, electrospun oxide NFs are regarded as very promising electrocatalysts for the WS.[53,54] Very recently, it has been demonstrated that HEO NFs can also be successfully prepared by ES.[55–57]

In this work, electrospun spinel-structured HEO NFs, based on equimolar (Cr,Mn,Fe,Co,Ni), (Cr,Mn,Fe,Co,Zn) and (Cr,Mn,Fe,Ni,Zn) combinations, are prepared and, for the first time, evaluated as OER electrocatalysts in alkaline electrolyte to investigate the influence of the different redox-active TM centres. To study the role of the catalyst morphology, (Cr,Mn,Fe,Co,Ni) HEO nanoparticles (NPs) are further produced *via* the sol–gel (SG) method for comparison. The results of the nanomaterials characterisation by complementary techniques are comparatively discussed to identify structural factors playing a crucial role on their electrocatalytic performance.

As previously shown,[57,58] both solution-based synthesis routes used here allow for the easy and low environmental-impact synthesis of homogeneous multicomponent oxides.[57,58] Besides, in the case of ES, the oxide NFs formed upon calcination from the as-spun precursor templates typically consist of interconnected crystalline grains of small size.[58–61] As the NF-composing oxide particles that can be easily detached from each other by dissolution in a solvent under sonication,[59] they could be used in the preparation of nanoparticulate electrocatalytic inks. Hence, this work may lead to important advances in the field of both nanostructured and ink-jet printable electrocatalysts.

Experimental procedure

Synthesis of the HEO-catalysts

Electrospun HEO-catalysts based on equimolar combinations of (Cr,Mn,Fe,Co,Ni), (Cr,Mn,Fe,Co,Zn) and (Cr,Mn,Fe,Ni,Zn) were prepared by following the procedures illustrated in detail in a previous work.[57] (Cr,Mn,Fe,Co,Ni) HEO NPs were further produced *via* the SG method to investigate the role of the catalyst morphology. Further details on the syntheses can be found in ESI.†

For an easy identification, the HEO-catalysts were labelled CN-NPs, CN-NFs, CZ-NFs and NZ-NFs, based on their morphology (NPs or NFs) and the varying cations in the TM combinations considered, namely (Co,Ni), (Co,Zn) and (Ni,Zn).

Physicochemical characterization

The physicochemical properties of the so-produced catalysts were investigated by scanning electron microscopy (SEM),

transmission electron microscopy (TEM), atomic force microscopy (AFM), X-ray powder diffraction (XRPD), micro-Raman spectroscopy (MRS) and X-ray photoelectron spectroscopy (XPS). A Phenom Pro-X scanning electron microscope spectrometer was used to study the catalyst texture and morphology. Higher resolution SEM images of CN-NPs sample were recorded using a JEOL JSM 7900F HR-FEG-SEM. An accelerating voltage of 15 kV was applied during the measurements. EDX elemental quantification was performed by means of an Oxford Instrument ULTIM MAX 40 probe. AFM images were recorded by means of a NT-MDT Integra Spectra C microscope operating in tapping mode, after dissolution of the NFs in acetone under sonication.

High-resolution TEM (HRTEM), high-angle annular dark-field scanning transmission electron microscopy (HAADF-STEM), selected-area electron diffraction (SAED) and energy dispersive X-ray spectroscopy (EDX) elemental mappings were carried out on a FEI Talos F200S scanning/transmission electron microscope, operated at 200 kV. XRPD patterns were recorded with a Bruker D2 diffractometer using Ni β-filtered Cu-K_α radiation source (λ = 0.1541 nm). Raman scattering was measured by a NTEGRA—Spectra SPM NT-MDT confocal microscope coupled to a solid-state laser operating at 2.33 eV (532 nm). The laser power was 250 μW at the sample surface. The scattered light from the sample, collected by means of a 100× Mitutoyo objective (NA = 0.75), was detected by a cooled ANDOR iDus CCD Camera. EnviroESCA (Specs) instrument equipped with an Al-K_α excitation source ($h\upsilon$ = 1486.6 eV) was utilized to perform the XPS studies. The spectra were recorded at RT working at a pressure of *ca.* 10^{-6} mbar. Survey and high-resolution spectra were acquired at 100 eV pass energy, 1.0 eV step^{-1}, and at 50 eV pass energy, 0.1 eV step^{-1}, respectively. Integration time was 0.1 s step^{-1}. Binding energy values (BE; uncertainty = ±0.2 eV) were corrected for charging assigning to the adventitious C 1s peak, attributed to adventitious hydrocarbons, the value of 284.8 eV.[58] XPS spectra were fitted using the Keystone software of Specs and applying a Shirley-type background function;[59] Specs supplied the sensitivity factors of integrated peak areas used for atomic percentages (at%) quantification. Further details on the instrumentation can be found elsewhere.[57,60,61]

Electrochemical measurements

Electrochemical measurements were performed using a three-electrode setup on a modulated speed rotator (Equilabrium SAS) with a rotating glassy carbon working electrode (A = 0.196 cm^2), a Pt spiral counter electrode and Ag/AgCl reference electrode. The working electrode was prepared by mixing 10 mg of active material in a solution consisting of 1800 μL of 2-propanol, 100 μL of ultra-pure water and 100 μL of Nafion (5 wt% Nafion in water/1-propanol, VWR) and 2 mg carbon black (MTI Corporation). The mixture was sonicated in an ultrasonic finger/homogenizer (Scientz-IID, Scientz) in an ice water bath for 30 min. For each measurement, a total of 15 μL of the solution (an aliquot) was dropped onto the surface of the working electrode (a catalyst loading of ∼0.38 mg cm^{-2}) and dried at room temperature. The electrocatalytic measurements were performed in an O_2-saturated electrolyte of 1 M KOH (90%, reagent grade, Sigma Aldrich) at 25 °C using a potentiostat (VSP, BioLogic GmbH). Linear sweep voltammetry (LSV) was performed at a sweep rate of 5 mV s^{-1} in a potential range from 1.0 to 1.8 V *vs.* RHE. iR-correction of LSV curves was done by subtraction of the electrolyte resistance derived from impedance spectroscopy. The Tafel slope was derived from LSV. The measured potentials are referred to the RHE, $E_{RHE} = E_{Ag/AgCl} + 0.059pH + E^{\theta}_{Ag/AgCl\ vs.\ RHE}$, where $E^{\theta}_{Ag/AgCl\ vs.\ RHE}$ is 0.1976 at 25 °C and the pH of the electrolyte was measured by pH meter as 13.3. The overpotential $\eta = E_{RHE} - 1.23$. IrO_2 (Alfa Aesar, Kandel, Germany, 99%) was used as reference material. Turnover frequency (TOF) values were calculated by assuming that every metal atom is involved in the catalysis process. The TOF = $jS/4Fn$, where j (mA cm^{-2}) is the measured current density at η = 373.15 mV (lowest overpotential at 10 mA cm^{-2} from CN-NFs), S is the surface area of the RDE disk (0.196 cm^2), the constant 4 means 4 electrons per mol of O_2, F is the Faraday's constant (96 485.3 C mol^{-1}), and n is the mole of the coated metal atoms on the electrode. The electrochemically active surface area (ECSA) was calculated *via* the equation ECSA = C_{dl}/C_s, where C_{dl} denotes electrochemical double-layer capacitance of the catalyst and C_s (0.04 mF cm^{-2}, according to literature[62,63]) indicates specific capacitance. C_{dl} was estimated *via* cyclic voltammetry (CV) measurement in a non-faradaic region using five different scan rates (5, 10, 20, 40 and 60 mV s^{-1}). The long-term stability was evaluated by performing CV measurements. 2306 CV cycles were applied to the electrode materials between 0.35 and 0.75 V *versus* Ag/AgCl at 50 mV s^{-1} in O_2-saturated electrolyte to observe the evolution of the current.

Results and discussion

Morphology

Fig. 1 and Fig. S2–S4 (ESI†) summarize the results of the SEM, TEM and HRTEM/EDX analyses on the HEO-catalysts produced by ES and SG method. SEM images (Fig. 1a–c) demonstrate that, for all TM combinations, micrometer-long, porous NFs are formed, upon calcination, from the polyacrylonitrile (PAN)/TM-acetates 1D templates. Their diameters vary in broad ranges (150–1850 nm, 110–1820 nm and 60–1280 nm for CN-NFs, CZ-NFs and NZ-NFs, respectively), with the centres of the distributions increasing in the order NZ-NFs (380 nm) < CZ-NFs (510 nm) < CN-NFs (660 nm), in full agreement with the results of previous studies.[57] (Cr,Mn,Fe,Co,Ni) HEO catalyst produced by the SG method consists of aggregates of NPs (Fig. 1d and Fig. S2, ESI†). TEM analysis (Fig. 1e–j) reveals that the NFs exhibit a hierarchical architecture. They consist of grains with a polyhedral shape and sizes ranging from a few tens to hundreds of nm, attached to each other to form a porous three-dimensional (3D) structure, as typical of several electrospun oxides.[60,63–69] Since the size of as-spun NFs constitutes a geometric constraint for the development of HEO grains, their size is generally smaller (and their size distribution usually narrow[60,70]) than that obtained under the same heat

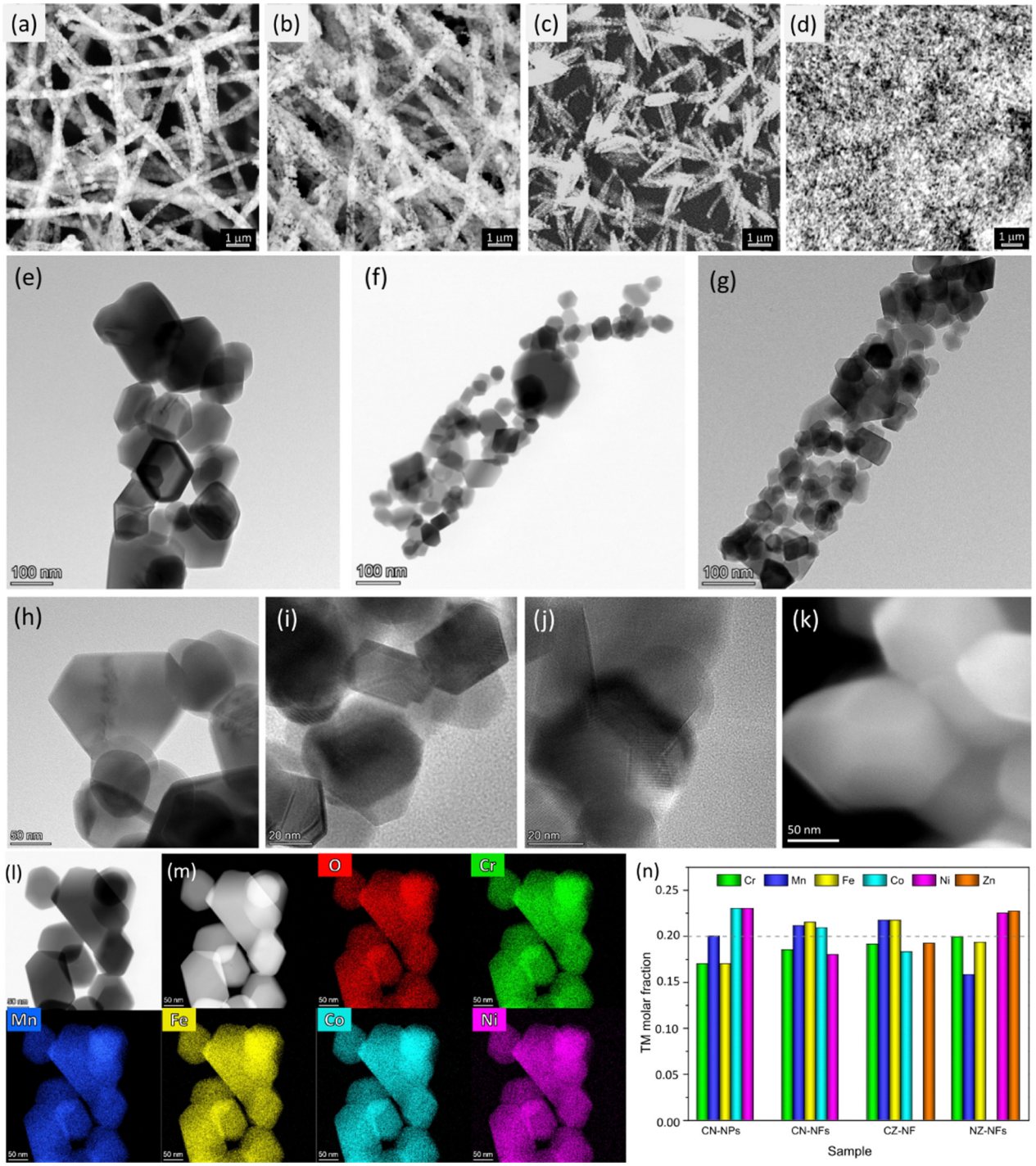

Fig. 1 Results of the SEM and HRTEM/STEM/EDX analyses on (a, e, h, k and l) CN-NFs, (b, f and g) CZ-NFs, (c, g and j) NZ-NFs and (d and k) CN-NPs. (a–d and k) SEM images, (e–j) HRTEM images; (l and m) STEM/EDX elemental maps of CN-NFs and (n) molar fraction of the TMs.

treatment conditions with other synthesis techniques, including SG (compare HEO grains in Fig. 1e and k). Moreover, as demonstrated in Fig. S5 (ESI†), the grains can be easily detached from each other. Thanks to their size, they are suitable for the preparation of electrocatalytic inks.

The diffraction rings in the SAED patterns for isolated NFs (see insets in Fig. S3, ESI†) prove that the oxide grains are crystalline; they have spinel structure and are randomly oriented. The lattice constants, as inferred from the geometrical phase analysis (GPA) of the crystal lattice fringes illustrated in detail in a previous paper,[61] increase in the order NZ-NFs (0.833 ± 0.003 nm) < CZ-NFs (0.836 ± 0.007 nm) < CN-NFs (0.843 ± 0.005 nm). This trend fully agrees with that reported for HEOs based on the same metal combinations synthesized by different

method.[71] The elemental mapping *via* STEM/EDX (Fig. 1l and m) confirms that the combustion reactions occurring during calcination give rise to the formation of HEOs from the interconnected TM-network built up *via* sol-chemistry from the reaction among acetates in the pristine solution. The spatial distribution of TMs and oxygen is homogeneous at the nanometer scale in all HEO-NFs and in NPs, as well. Besides, the compositional analysis confirms that TM combinations very close to the nominal ones are achieved (Fig. 1n).

The rapid rise in temperature during calcination causes the precursor PAN/TM-acetates NFs to experience a large temperature gradient along the radial direction. As a result, the HEO-NFs exhibit mostly a tube-like structure, as expected.[61,71] Previous studies on HEO-NFs produced under similar conditions have shown that their cross section, as resulting from the projection analysis of the EDX elemental maps,[61] varies with the TM combination. In particular, CN-NFs are quasi-solid (Fig. S4a, ESI†), CZ-NFs are irregularly hollow (Fig. S4b, ESI†), and NZ-NFs are hollow (Fig. S4c, ESI†).

Crystalline phase and surface composition of the HEO catalysts

Fig. 2a shows the XRPD patterns of the catalysts. Regardless of their morphology and composition, only the reflections from the crystallographic planes of the face-centred cubic (fcc) spinel structure are observed (JCPDS no. 22-1084),[73–77] indicating that pure single-phase solid solutions are formed in all samples, in full agreement with the evidences of the SAED analysis and the results of previous studies, as well.[57,61] The average size of the HEO crystallites, as calculated from the full width at half maximum (FWHM) of the most intense reflection through the Scherrer's equation, $d = k\lambda/\beta\cos\theta$ (where k, λ, β and θ denote the shape factor, the wavelength of X-ray radiation, the FWHM in radians and the Bragg's angle, respectively),[78] decreases in the order CN-NPs (124 nm) > NZ-NFs (99 nm) > CN-NFs (97 nm) > CZ-NFs (84 nm).

In agreement with a previous study,[61] the lattice parameter of the cubic cell, as inferred from Rietveld analysis (not shown for briefness), increases in the order CN-NFs (8.3215(8) Å) < NZ-NFs (8.3256(6) Å) < CZ-NFs (8.3712(8) Å). This trend is different with respect to that of the *a*-values estimated from HRTEM (NZ-NFs < CZ-NFs < CN-NFs). This is not surprising due to the different areas sampled by XRPD and HRTEM. In particular, the smaller value of the lattice constant obtained for CN-NFs might reflect the occurrence of compressive strains, previously observed along the free edges of some of the grains that compose the fibers.[61]

The spatial homogeneity of the catalysts is evaluated by measuring Raman scattering from several random locations on each specimen (not shown for briefness). No appreciable differences in the positions of the bands and in their relative intensities are observed at the probed locations, confirming that pure single-phase HEOs are formed[73] regardless of the synthesis route and the TM combination, in agreement with the results of both the XRPD analysis and previous studies.[57,61]

Fig. 2b displays the micro-Raman spectra, as obtained by averaging the spectra collected at random locations. The five phonon modes predicted by the factor group analysis for the fcc spinels (space group: $Fd\bar{3}m$)[18,22,79–81] are detected in all HEOs, namely the $F_{2g}(1)$, E_g, $F_{2g}(2)$, $F_{2g}(3)$ and A_{1g} modes, centred at 170–180 cm^{-1}, 350–360 cm^{-1}, 510–520 cm^{-1}, 550–590 cm^{-1} and 610–660 cm^{-1}, respectively. They involve the motions of oxygen anions along the cubic space diagonals[82,83] Besides the five normal modes, the A'_{1g} mode clearly contributes to the Raman intensity in the higher-frequency region of the spectra of $(Cr_{0.2}Mn_{0.2}Fe_{0.2}Co_{0.2}Ni_{0.2})_3O_4$ NPs and NFs, in agreement with the literature.[72,77] The spectral feature, appearing as a shoulder in the spectrum of CN-NFs, is better resolved in that of CN-NPs, which closely reminds of that (Cr,Mn,Fe,Co,Ni) HEO NPs synthesized *via* the reverse co-precipitation approach[77] and the solid-state reaction route.[72] The larger average size of the HEO crystallites (*i.e.* larger coherence length) in NPs (124 against 97 nm in NFs) may account for this difference. Its detection is indicative of the occurrence of inversion in the

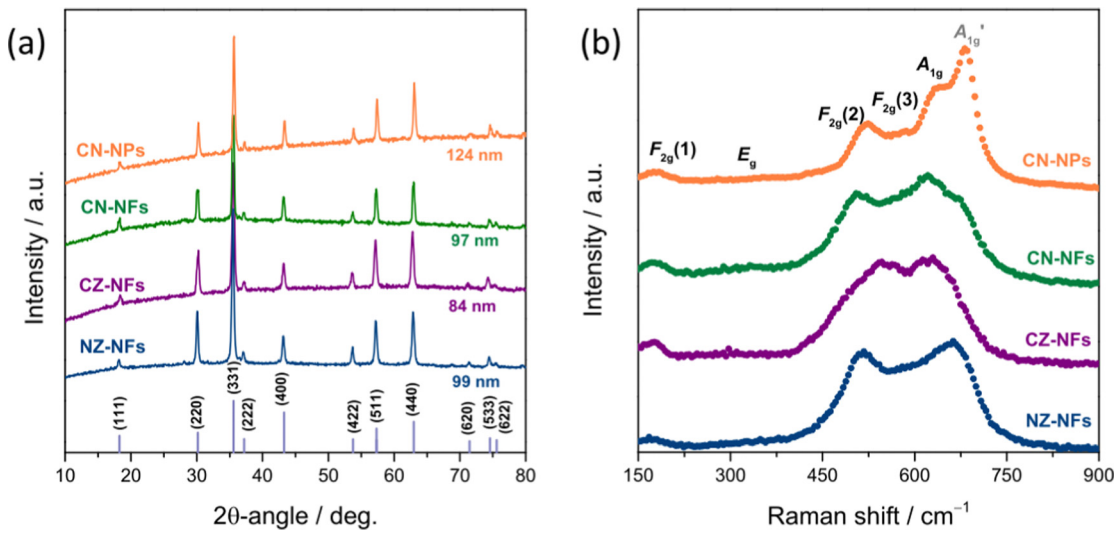

Fig. 2 (a) XRPD patterns and (b) micro-Raman spectra of the HEO-catalysts. The average size of the HEO crystallites is also reported in plot (a).

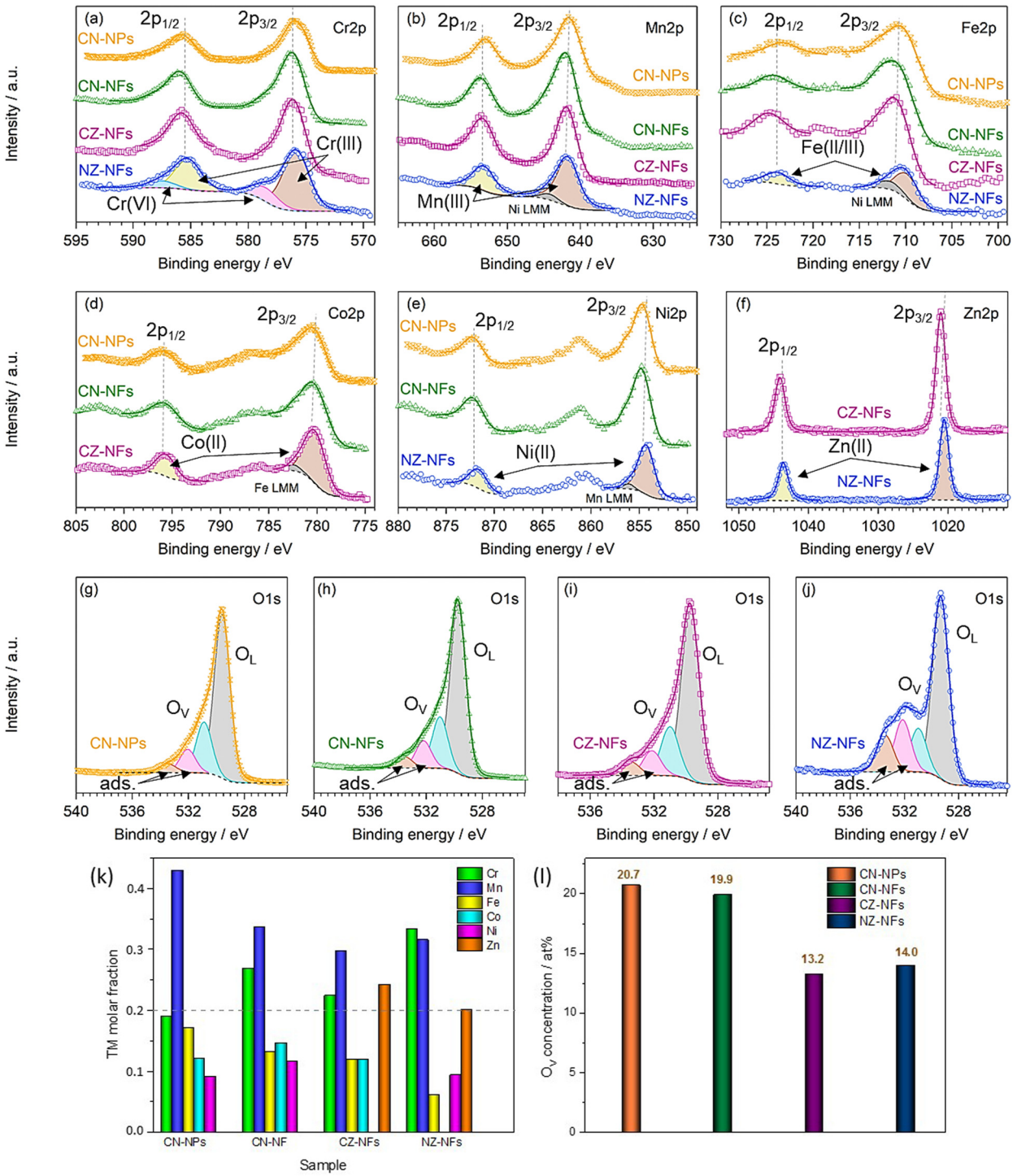

Fig. 3 High-resolution XPS spectra and fitting of (a) Cr 2p, (b) Mn 2p, (c) Fe 2p, (d) Co 2p, (e) Ni 2p, (f) Zn 2p and (g–j) O 1s core levels and resulting (k) TM molar fraction in the combination ($Cr_{0.2}Mn_{0.2}Fe_{0.2}M'_{0.2}M''_{0.2}$), where M′M″ denotes the metal pairs CoNi, CoZn and NiZn, and (l) O_V concentration. Labels indicate the peak assignment: O_V = oxygen vacancies; O_L = lattice oxygens; ads. = adsorbed or chemisorbed oxygen species (*e.g.*, O_2 or H_2O).

oxide lattice.[22,73,84] Inversion also occurs to a minor extent in the remaining HEOs. For an in-depth discussion on the inversion-degree in the HEO-NFs and of its effect on their MRS spectra and magnetic properties, see ref. 61.

Fig. 3a–j shows the high-resolution XPS spectra (HRXPS) of Cr 2p, Mn 2p, Fe 2p, Co 2p, Ni 2p, Zn 2p and O 1s core levels and their fitting. From the analysis of the HRXPS spectra, it comes out that chromium is mainly present as Cr(III). In addition, Cr^{6+} surface species are present, as reported also for HEO-NPs synthesized *via* different methods.[27,85,86] Manganese appears with 3+ oxidation state, whereas iron is present as both Fe(III) and Fe(II). Although the similar BE-values make Co(II) and Co(III)

difficult to distinguish,[87,88] the strong satellite peaks appearing in the spectra of Co 2p core levels would suggest that cobalt is mainly present as Co(II). Nickel and zinc both appear with 2+ oxidation state. An in-depth discussion of the HRXPS spectra of (Cr,Mn,Fe,Co,Ni), (Cr,Mn,Fe,Co,Zn) and (Cr,Mn,Fe,Ni,Zn) HEO-NFs can be found elsewhere.[61] Table S1 (ESI†) reports the atomic concentrations of the surface species. It is worthwhile noticing that the detection of LMM Auger lines, superimposed on the $2p_{3/2}$ spin orbit component of Mn, Fe, Co and Ni, increases the uncertainty in the estimation of the atomic concentrations of Mn, Fe, Co and Ni surface species. Fig. 3k shows the molar fraction of TMs on the catalyst surface. Different from the STEM/EDX analysis (Fig. 1n), the XPS analysis reveals significant deviations from equimolarity for all TM combinations, with the relative concentration of some surface species (Mn^{3+} in the NPs and Mn^{3+}/Cr^{3+} in the NFs) largely exceeding the nominal 0.2 value at expenses of that of the remaining ones. Such TM distribution might reflect the preference of spinel oxides to expose mainly octahedral sites on the surface.[17] Qualitatively, this would be not in contrast neither with the distributions of cations (sketched in Fig. 4), previously proposed by Ponti *et al.*[61] for $(Cr_{0.2}Mn_{0.2}Fe_{0.2}M'_{0.2}M''_{0.2})_3O_4$ NFs (with M′M″ indicating the metal pairs CoNi, CoZn and NiZn) based on the optimization of the octahedral stabilization under the constraint of electroneutrality, nor with that demonstrated by Sarkar *et al.*[89] for micrometer-sized $(Cr_{0.2}Mn_{0.2}Fe_{0.2}Co_{0.2}Ni_{0.2})_3O_4$ HEO using X-ray, Mössbauer, and neutron techniques. The occurrence of surface reconstruction processes[17] might account for the different details among all samples.

With reference to the cation distributions shown in Fig. 4, it is worthwhile noticing that, on one hand, the larger fraction of Fe^{3+}/Co^{3+} cations at the tetrahedral 8a sites would result in greater inversion degree (λ) for $(Cr_{0.2}Mn_{0.2}Fe_{0.2}Co_{0.2}Ni_{0.2})_3O_4$ NPs and NFs, compared to $(Cr_{0.2}Mn_{0.2}Fe_{0.2}Co_{0.2}Zn_{0.2})_3O_4$ and $(Cr_{0.2}Mn_{0.2}Fe_{0.2}Ni_{0.2}Zn_{0.2})_3O_4$ NFs (0.8 against 0.4),[61] in agreement with the results of MRS analysis; in turn, this would reflect in higher bulk conductivity.[23,24] On the other hand, the larger fraction of tetrahedral Fe^{3+}/Co^{3+} cations would translate into increased octahedral occupation by Co/Ni (to ensure electroneutrality) in the CN-catalysts; this would be beneficial for their OER performance due to the tendency of the charge of O^{2-} anion to shift toward the redox-active TMs occupying octahedral instead of tetrahedral sites.[17,26]

The fitting of the HRXPS spectra of O 1s core level evidences that, besides oxygen anions belonging to the HEO lattice,[90–93] oxygen vacancies (O_Vs),[90–93] and adsorbed or chemisorbed oxygen species, such as O_2 or H_2O, are present on the catalyst surface,[94–96] in line with other reports on HEOs[27] and the results of previous studies.[61] Being generally able to promote the adsorption of oxygen intermediates (*e.g.* O*, OH*, OOH*),[17] thus enhancing the electrocatalytic performance,[24] also the native defects of O_Vs play a crucial role. Their concentration is higher in catalysts that expose both Co and Ni on their surface, *i.e.* in CN-NPs and CN-NFs, than in those that expose only one of these catalytically active centres (Fig. 3l).

Electrochemical performance

The OER performance of the HEO-based electrocatalysts was tested in an O_2-saturated 1 M KOH electrolyte solution using a three-electrode setup. In order to evaluate the catalytic activities of CZ-NFs, NZ-NFs, CN-NFs and CN-NPs towards the OER, their polarization curves were measured and investigated by LSV. The linear sweep voltammograms of the spinel-type HEOs and IrO_2 reference material are shown in Fig. 5a. The results highlight that the HEOs considered exhibit different catalytic performance. As a general trend, the lower the overpotential, the better the catalytic activity since a lower overvoltage is required to obtain the same current density.[44,97] At 10 mA cm^{-2}, the overpotential decreases in the order CZ-NFs (393 mV) > NZ-NFs (376 mV) > CN-NPs (373 mV) > CN-NFs (365 mV) > IrO_2

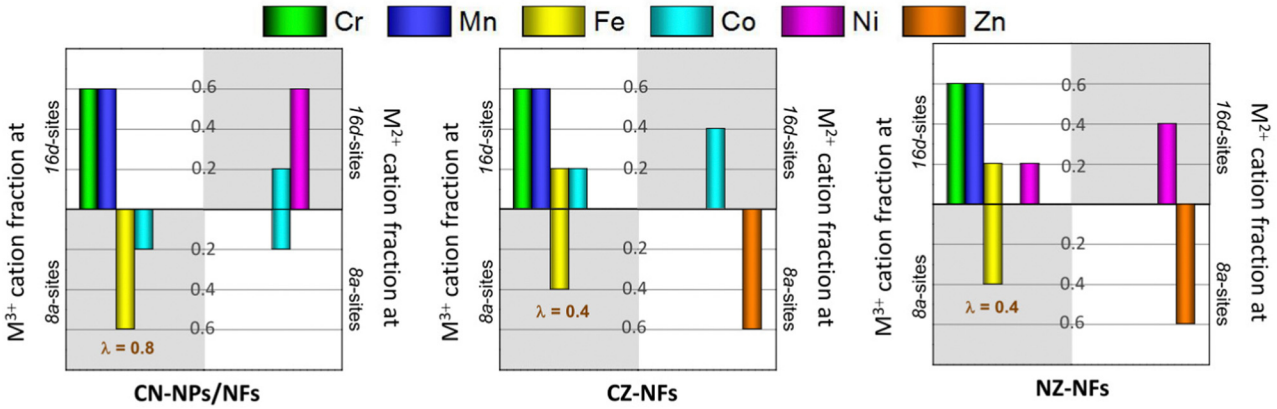

Fig. 4 Cation distributions for $(Cr_{0.2}Mn_{0.2}Fe_{0.2}M'_{0.2}M''_{0.2})_3O_4$ catalysts (with M′M″ standing for the metal pairs CoNi, CoZn and NiZn) that satisfy electroneutrality of the spinel phase and optimize octahedral stabilization (adapted from the results reported in ref. 52). The total molar fraction of each cation is 0.6, regardless of its oxidation state (2+ or 3+) and the type of site occupied (tetrahedral or octahedral). The inversion degree (λ) is also reported. In CN-catalysts, cations are randomly distributed with $(Cr_{0.6}Mn_{0.6}Co_{0.2}Ni_{0.6})$ in 16d sites and $(Fe_{0.6}Co_{0.4})$ in 8a sites; in CZ-NFs, $(Cr_{0.6}Mn_{0.6}Fe_{0.2}Co_{0.6})$ occupy octahedral sites and $(Fe_{0.4}Zn_{0.6})$ occupy tetrahedral sites; in NZ-NFs, the cation distribution is analogous to that of CZ-NFs with Ni-in place of Co-cations.

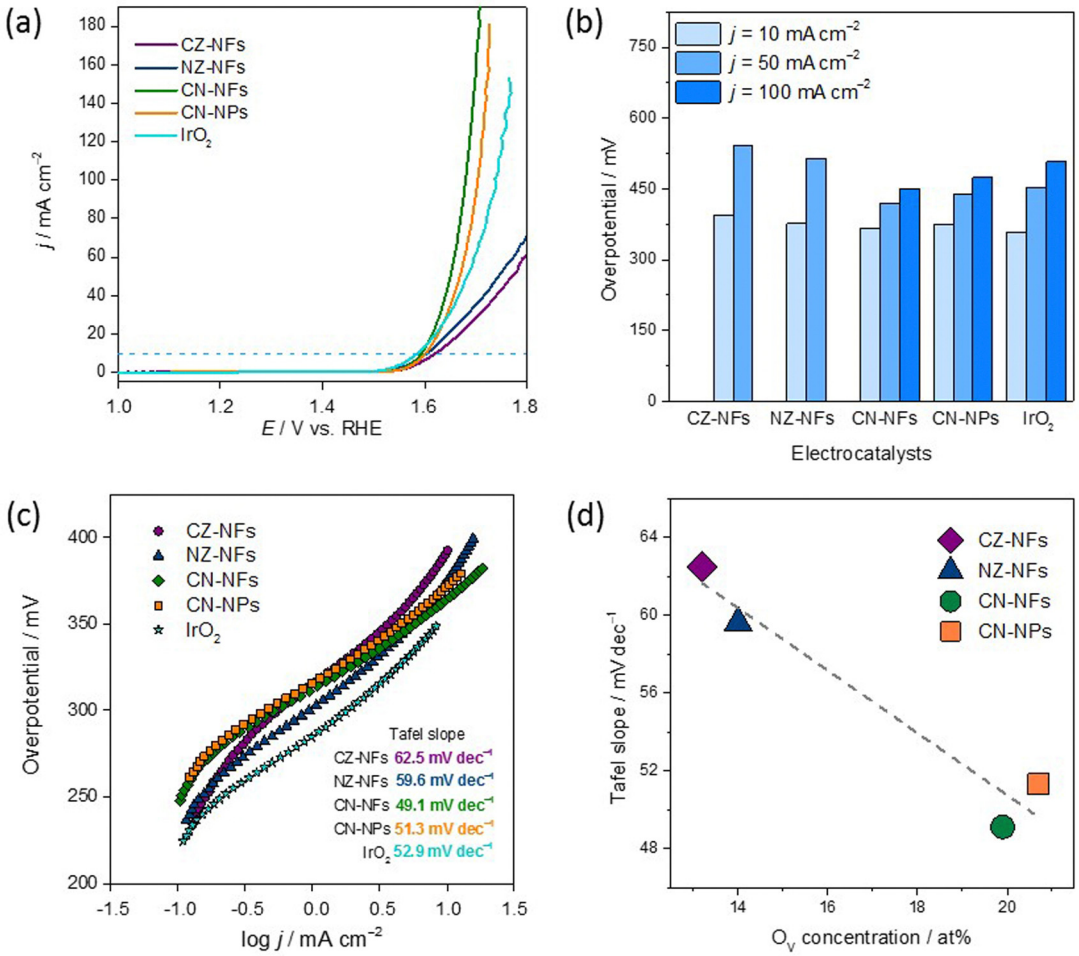

Fig. 5 (a) Linear sweep voltammograms of the spinel-type high-entropy oxides (CZ-NFs, NZ-NFs, CN-NFs, and CN-NPs) and IrO_2 reference material during OER in O_2-saturated 1 M KOH, the dashed line highlights the values for the overpotential at 10 mA cm^{-2}. (b) Comparison of the OER overpotentials at different current densities. (c) Tafel slopes of the considered electrocatalysts. (d) Tafel slopes of the HEOs as a function of the O_V-concentration (a line is drawn to guide the eye).

0(358 mV). Thus, the catalytic activity improves in the opposite order. Table S2 (ESI†) compares the activities of HEO-based electrocatalysts.

It is worth noting that HEOs based on equimolar combinations comprising zinc, namely (Cr,Mn,Fe,Co,Zn) and (Cr,Mn,Fe,Ni,Zn), exhibit worse catalytic performance than both HEOs (NPs and NFs) based on the Zn-free equimolar combination (Cr,Mn,Fe,Co,Ni). In turn, the overpotentials of CN-NFs and CN-NPs are comparable to those reported in the literature for both for catalysts based on HEOs produced by different methods[27] and for catalysts based on low-entropy oxides.[29,98] Besides, at 10 mA cm^{-2}, the overpotentials of CN-NFs and CN-NPs slightly exceed that of IrO_2, but at higher current densities (50 and 100 mA cm^{-2}), the situation reverses and, regardless of their morphology, (Cr,Mn,Fe,Co,Ni)-based HEOs show lower overvoltages than IrO_2 (Fig. 5b).

As usual,[97] to evaluate the reaction kinetics of spinel-type HEOs and IrO_2, the slopes of the Tafel curves (Fig. 5c) obtained from the collected LSV curves (Fig. 5a) were calculated. As a general trend, the lower the Tafel slope, the faster the reaction kinetics.[97] The lower Tafel slope indicates an easier acceleration of electron transfer and electron migration during the catalytic process, allowing the catalyst to produce larger current densities at the same potential. CZ-NFs and NZ-NFs exhibit Tafel slopes (62.5 and 59.6 mV dec^{-1}, respectively) comparable to that reported for high-entropy amorphous metal oxide FeCoNiMn/Sn/Cu (64.5–73.9 mV dec^{-1}) produced by liquid phase non-equilibrium reduction method[97] and defective $Mg_{0.2}Co_{0.2}Ni_{0.2}Cu_{0.2}Zn_{0.2}O$ prepared by electrospinning (61.4 mV dec^{-1}).[28] Remarkably, the Tafel slopes of CN-NFs and CN-NPs (49.1 and 51.3 mV dec^{-1}, respectively) are lower not only than that of IrO_2 (60.2 mV dec^{-1}), but also lower than those of porous CoCrFeNiMo HEA prepared by microwave sintering (59.0 mV dec^{-1})[44] and $(Cr_{0.2}Mn_{0.2}Fe_{0.2}Co_{0.2}Ni_{0.2})_3O_4$ particles prepared by solid state reaction (54.5 mV dec^{-1})[48] and reverse co-precipitation approach (100 mV dec^{-1}).[77] This is an important finding because improving OER kinetics would favour a broad market penetration of alkaline WS technology.[16]

Considering that OER is a morphology-dependent catalytic reaction, the ECSA was determined using the C_{dl} estimated by

CV measurements in a non-faradaic region (Fig. S6, ESI†). The C_{dl} values of CZ-NFs, NZ-NFs, CN-NFs, and CN-NPs are 3.87, 1.16, 1.45, and 1.94 mF cm^{-2}, respectively; and the ECSA values are 96.8, 29.0, 36.3, and 48.5 cm^2, respectively. The LSV curves were then normalized to the ECSA to evaluate the intrinsic activity (Fig. S7, ESI†). CN-NFs show the highest intrinsic catalytic activity. To further evaluate the OER catalyst rates, the TOF values of the four electrocatalysts were estimated, assuming that all metal ions are catalytically active. The TOF values at η_{365mV} (see Fig. S8 and Table S3, ESI†) further confirmed the better OER performance of CN-NFs (0.034 s^{-1}) compared to CN-NPs (0.025 s^{-1}), CZ-NFs (0.026 s^{-1}) and NZ-NFs (0.018 s^{-1}). The results of the ECSA and TOF evaluation show that CZ-NFs perform slightly better than CN-NPs, which initially suggested a better activity in terms of current density relative to the electrode surface. This indicates that the surface morphology has a positive influence on the catalytic activity, although the difference between CZ-NFs and CN-NPs is very small. However, combining both, the selection of elements with an optimized interface as it is the case for CN-NFs (Fig. 5a), shows that this leads to a significantly better OER active material.

To investigate the long-term electrochemical stability of CN-NFs, repeated CV measurements were performed in an electrolyte saturated with O_2 in the OER range (Fig. S9, ESI†). This procedure allows studying the catalyst aging during long-term CV tests. From the first to the 100th cycle, a slight gradual decrease in the final current at 1.8 V *vs.* RHE can be seen, followed by a sharp increase at 500 cycles. The corresponding values for the 1st, 50th, 100th, and 500th cycles are 1.8, 1.6, 1.5, and 5.9 mA cm^{-2}, respectively. Thereafter, the current density decreases drastically until the complete failure of the electrode material. The initial slight decrease may indicate a restructuring of the active material and activation, as there was a sharp increase in current density thereafter. The later decrease, on the other hand, shows signs of material failure due to decomposition processes.

The generally good OER performance of all spinel-type HEO materials probably benefits from the large molar fractions of Mn^{3+} and Cr^{3+} (overall always >1.2) surface species occupying octahedral 16d sites in the lattice,[61] which are thought to contribute significantly to the electrocatalytic activity of HEOs.[27] However, this does not explain the difference in electrocatalytic activity among the samples. The poorer catalytic activity of CZ-NFs and NZ-NFs could be attributed to the occupation of the tetrahedral sites mainly by the Zn^{2+} ions (Fig. 4), whose larger ionic radius (60 pm against 49 pm for fourfold-coordinated Fe^{3+} ions[99]) might promote structure destruction, resulting in low and unstable OER activity. Moreover, as discussed above, in CZ-NFs and NZ-NFs the fraction of M^{3+}-cations (Fe^{3+}) in the tetrahedral sites is expected to be lower than in Zn-free catalysts, featured by higher inversion degree (Fig. 4). In CN-NPs/NFs, the larger fraction of tetrahedral M^{3+}-cations (Fe^{3+}/Co^{3+}) with lower coordination to lattice O translates into higher occupation of octahedral sites by Co^{2+} and Ni^{2+} redox-centres that are more active.[8] In turn, according to the most recent assessments on TM-based catalysts,[17,26,100] this leads to improved OER performance due to the tendency of the charge of the O^{2-}-anion to shift toward the redox-active TMs occupying octahedral rather than tetrahedral sites. The higher concentration of O_Vs (Fig. 5d) also contributes to enhance the catalytic activity of CN-NPs/NFs since oxygen vacancies promote the adsorption of oxygen intermediates during the catalytic process.

Conclusions

Spinel-type HEO nanofibers, based on equimolar (Cr,Mn,Fe,Co,Ni), (Cr,Mn,Fe,Co,Zn) and (Cr,Mn,Fe,Ni,Zn) combinations, are synthesised by electrospinning and evaluated as OER electrocatalysts in alkaline electrolyte together with (Cr,Mn,Fe,Co,Ni) HEO nanoparticles prepared *via* the sol–gel method.

The results of the electrochemical testing highlight that, although all HEOs show generally good activity and fast kinetics, the best performance pertains to $(Cr_{0.2}Mn_{0.2}Fe_{0.2}Co_{0.2}Ni_{0.2})_3O_4$ electrocatalysts. Remarkably, regardless of their morphology, the Tafel slopes of these catalysts (51.3 mV dec^{-1} for nanoparticles and 49.1 mV dec^{-1} for nanofibers) are lower than that of IrO_2 reference material (52.9 mV dec^{-1}), which may be helpful for market penetration of alkaline WS technology. Based on the most recent assessments on spinel-type catalysts, their behaviour is understood as the effect of the higher concentration of oxygen vacancies on their surface and the higher occupation of octahedral sites by redox-active Co^{2+} and Ni^{2+} centres.

Thanks to the possibility of easily separating the small-sized grains that make up the fibres from each other, electrospun HEOs have great potential as inkjet printable electrocatalysts.

Author contributions

Claudia Triolo: data curation, formal analysis, investigation, validation, methodology. Simon Schweidler: data curation, formal analysis, investigation, validation, methodology, writing – original draft, resources. Ling Lin: data curation, formal analysis, investigation, validation, methodology. Gioele Pagot: data curation, formal analysis, investigation, validation, methodology. Vito Di Noto: data curation, formal analysis, investigation, validation, methodology. Ben Breitung: data curation, formal analysis, investigation, validation, methodology. Saveria Santangelo: conceptualization, visualization, formal analysis, writing – original draft, writing – review & editing, supervision.

Data availability

The data that support the plots in this paper and other findings of this study are available from the corresponding author upon reasonable request.

Conflicts of interest

There are no conflicts to declare.

Acknowledgements

Simon Schweidler acknowledges the support from EPISTORE project funded by the European Union's Horizon 2020 research and innovation program under grant agreement no. 101017709. Ling Lin acknowledges financial support from the China Scholarship Council (CSC). The work at the University of Padova was funded by the Italian Ministry of University and Research under the project "Alkaline membranes and (platinum group metals)-free catalysts enabling innovative, open electrochemical devices for energy storage and conversion – AMPERE", FISR 2019 project.

Notes and references

1 P. P. Edwards, V. L. Kuznetsov and W. I. David, *Philos. Trans. R. Soc., A*, 2007, **365**, 1043.
2 T. N. Veziroğlu and S. Şahi, *Energy Convers. Manage.*, 2008, **49**, 1820.
3 A. Pareek, R. Dom, J. Gupta, J. Chandran, V. Adepu and P. H. Borse, *Mater. Sci. Energy Technol.*, 2020, **3**, 319.
4 D. K. Bora, A. Braun and E. C. Constable, *Energy Environ. Sci.*, 2013, **6**, 407.
5 R. D. Tentu and S. Basu, Photocatalytic water splitting for hydrogen production, *Curr. Opin. Electrochem.*, 2017, **5**, 56.
6 U. Gupta and C. N. R. Rao, *Nano Energy*, 2017, **41**, 49.
7 S. Wang, A. Lu and C. J. Zhong, *Nano Convergence*, 2021, **8**, 4.
8 S. A. Patil, S. Cho, Y. Jo, N. K. Shrestha, H. Kim and H. Im, *Chem. Eng. J.*, 2021, **426**, 130773.
9 N. K. Shrestha, S. A. Patil, S. Cho, Y. Jo, H. Kim and H. Im, *J. Mater. Chem. A*, 2020, **8**, 24408.
10 F. Luo, L. Guo, Y. Xie, J. Xu, K. Qu and Z. Yang, *Appl. Catal., B*, 2020, **279**, 119394.
11 Y. Li, Y. Sun, Y. Qin, W. Zhang, L. Wang, M. Luo, H. Yang and S. Guo, *Adv. Energy Mater.*, 2020, **10**, 1903120.
12 J. Zhou, J. Li, L. Zhang, S. Song, Y. Wang, X. Lin, S. Gu, X. Wu, T. C. Weng, J. Wang and S. Zhang, *J. Phys. Chem. C*, 2018, **122**, 14447.
13 X. P. Li, C. Huang, W. K. Han, T. Ouyang and Z. Q. Liu, *Chin. Chem. Lett.*, 2021, **32**, 2597.
14 H. Liu, C. Xi, J. Xin, G. Zhang, S. Zhang, Z. Zhang, Q. Huang, J. Li, H. Liu and J. Kang, *Chem. Eng. J.*, 2021, **404**, 126530.
15 S. Meng, S. Sun, Y. Liu, Y. Lu and M. Chen, *J. Colloid Interface Sci.*, 2022, **624**, 433–442.
16 E. Fabbri, A. Habereder, K. Waltar, R. Kötz and T. J. Schmidt, *Catal. Sci. Technol.*, 2014, **4**, 3800.
17 Y. Zhou, S. Sun, C. Wei, Y. Sun, P. Xi, Z. Feng and Z. J. Xu, *Adv. Mater.*, 2019, **31**, 1902509.
18 Z. M. Stanojević, N. Romčević and B. Stojanović, *J. Eur. Ceram. Soc.*, 2007, **27**, 903.
19 M. Stygar, J. Dąbrowa, M. Moździerz, M. Zajusz, W. Skubida, K. Mroczka, K. Berent, K. Świerczek and M. Danielewski, *J. Eur. Ceram. Soc.*, 2020, **40**, 1644.
20 B. Issa, I. M. Obaidat, B. A. Albiss and Y. Haik, *Int. J. Mol. Sci.*, 2013, **14**, 21266.
21 M. A. Laguna-Bercero, M. L. Sanjuán and R. I. Merino, *J. Phys.: Condens. Matter*, 2007, **19**, 186217.
22 V. D' Ippolito, G. B. Andreozzi, D. Bersani and P. P. Lottici, *J. Raman Spectrosc.*, 2015, **46**, 1255.
23 P. F. Ndione, Y. Shi, V. Stevanovic, S. Lany, A. Zakutayev, P. A. Parilla, J. D. Perkins, J. J. Berry, D. S. Ginley and M. F. Toney, *Adv. Funct. Mater.*, 2014, **24**, 610.
24 L. I. Granone, R. Dillert, P. Heitjans and D. W. Bahnemann, *ChemistrySelect*, 2019, **4**, 1232.
25 S. Wahl, S. M. El-Refaei, A. G. Buzanich, P. Amsalem, K. S. Lee, N. Koch, M. L. Doublet and N. Pinna, *Adv. Energy Mater.*, 2019, **9**, 1900328.
26 S. Sun, Y. Sun, Y. Zhou, S. Xi, X. Ren, B. Huang, H. Liao, L. P. Wang, Y. Du and Z. J. Xu, *Angew. Chemie*, 2019, **131**, 6103.
27 M. Einert, M. Mellin, N. Bahadorani, C. Dietz, S. Lauterbach and J. P. Hofmann, *ACS Appl. Energy Mater.*, 2022, **5**, 717.
28 F. Liu, M. Yu, X. Chen, J. Li, H. Liu and F. Cheng, *Chin. J. Catal.*, 2022, **43**, 122.
29 Y. Zhang, W. Dai, P. Zhang, T. Lu and Y. Pan, *J. Alloys Compd.*, 2021, **868**, 159064.
30 A. Krishnan, R. Ajay, J. Anakha and U. K. Namboothiri, *Surf. Interfaces*, 2022, **30**, 101942.
31 X. Yang, S. Liping, L. Qiang, H. Lihua and Z. Hui, *J. Mater. Chem. A*, 2022, **10**, 17633.
32 L. He, H. Kang, G. Hou, X. Qiao, X. Jia, W. Qin and X. Wu, *Chem. Eng. J.*, 2023, **460**, 141675.
33 J. Bao, X. Zhang, B. Fan, J. Zhang, M. Zhou, W. Yang, X. Hu, H. Wang, B. Pan and Y. Xie, *Angew. Chem.*, 2015, **127**, 7507.
34 J. Sun, N. Guo, Z. Shao, K. Huang, Y. Li, F. He and Q. Wang, *Adv. Energy Mater.*, 2018, **8**, 1800980.
35 M. Li, M. Song, W. Ni, Z. Xiao, Y. Li, J. Jia, S. Wang and Y. Wang, *Chin. Chem. Lett.*, 2023, **34**, 107571.
36 C. Wei, Z. Feng, G. G. Scherer, J. Barber, Y. Shao-Horn and Z. J. Xu, *Adv. Mater.*, 2017, **29**, 1606800.
37 Y. Zhou, S. Sun, J. Song, S. Xi, B. Chen, Y. Du, A. C. Fisher, F. Cheng, X. Wang, H. Zhang and Z. J. Xu, *Adv. Mater.*, 2018, **30**, 1802912.
38 M. Fu, X. Ma, K. Zhao, X. Li and D. Su, *iScience*, 2021, **24**, 102177.
39 H. Li, H. Zhu, S. Zhang, N. Zhang, M. Du and Y. Chai, *Small Struct.*, 2020, **1**, 2000033.
40 H. J. Qiu, G. Fang, J. Gao, Y. Wen, J. Lv, H. Li, G. Xie, X. Liu and S. Sun, *ACS Mater. Lett.*, 2019, **1**, 526.
41 Z. J. Chen, T. Zhang, X. Y. Gao, Y. J. Huang, X. H. Qin, Y. F. Wang, K. Zhao, X. Peng, C. Zhang, L. Liu, M. H. Zeng and H. B. Yu, *Adv. Mater.*, 2021, **33**, 2101845.
42 K. Li and W. Chen, *Mater. Today Energy*, 2021, **20**, 100638.
43 H. Li, J. Lai, Z. Li and L. Wang, *Adv. Funct. Mater.*, 2021, **31**, 2106715.
44 J. Tang, J. L. Xu, Z. G. Ye, X. B. Li and J. M. Luo, *J. Mater. Sci. Technol.*, 2021, **79**, 171.
45 L. Sharma, N. K. Katiyar, A. Parui, R. Das, R. Kumar, C. S. Tiwary, A. K. Singh, A. Halder and K. Biswas, *Nano Res.*, 2021, **15**, 4799.

46 Y. Zhang, D. Wang and S. Wang, *Small*, 2022, **18**, 2104339.
47 T. X. Nguyen, Y. C. Liao, C. C. Lin, Y. H. Su and J. M. Ting, *Adv. Funct. Mater.*, 2021, **31**, 2101632.
48 Z. Sun, Y. Zhao, C. Sun, Q. Ni, C. Wang and H. Jin, *Chem. Eng. J.*, 2022, **431**, 133448.
49 D. Stenzel, B. Zhou, C. Okafor, M. V. Kante, L. Lin, G. Melinte, T. Bergfeldt, M. Botros, H. Hahn, B. Breitung and S. Schweidler, *Front. Energy Res.*, 2022, **10**, 942314.
50 Z. Li and C. Wang, *One-dimensional nanostructures: electrospinning technique and unique nanofibers*, Springer Berlin Heidelberg, New York Dordrecht London, 2013, pp. 15–29.
51 Q. Liu, J. Zhu, L. Zhang and Y. Qiu, *Renewable Sustainable Energy Rev.*, 2018, **81**, 1825.
52 S. Santangelo, *Appl. Sci.*, 2019, **9**, 1049.
53 L. Zhang, H. Zhao, S. Xu, Q. Liu, T. Li, Y. Luo, S. Gao and X. Sun, *Small Struct.*, 2021, **2**, 2000048.
54 Z. Zhang, X. Wu, Z. Kou, N. Song, G. Nie, C. Wang, F. Verpoort and S. Mu, *Chem. Eng. J.*, 2022, **428**, 131133.
55 W. Zhao, F. Yang, Z. Liu, H. Chen, Z. Shao, X. Zhang, K. Wang and L. Xue, *Ceram. Int.*, 2021, **47**(20), 29379–29385.
56 Y. Xing, W. Dan, Y. Fan and X. A. Li, *J. Mater. Sci. Technol.*, 2022, **103**, 215.
57 B. Petrovičovà, W. Xu, M. G. Musolino, F. Pantò, S. Patanè, N. Pinna, S. Santangelo and C. Triolo, *Appl. Sci.*, 2022, **12**, 5965.
58 D. Briggs and M. P. Seah, *Practical surface analysis: Auger and X-ray photoelectron spectroscopy*, John Wiley & Sons, New York, 2nd edn, 1990.
59 D. A. Shirley, *Phys. Rev. B: Condens. Matter Mater. Phys.*, 1972, **5**, 4709.
60 F. Pantò, Z. Dahrouch, A. Saha, S. Patanè, S. Santangelo and C. Triolo, *Appl. Surf. Sci.*, 2021, **557**, 149830.
61 A. Ponti, C. Triolo, B. Petrovičovà, A. M. Ferretti, G. Pagot, W. Xu, V. D. Noto, N. Pinna and S. Santangelo, *Phys. Chem. Chem. Phys.*, 2023, **25**, 2212.
62 C. C. L. McCrory, S. Jung, J. C. Peters and T. F. Jaramillo, *J. Am. Chem. Soc.*, 2013, **135**, 16977.
63 M. Cui, C. Yang, B. Li, Q. Dong, M. Wu, S. Hwang, H. Xie, X. Wang, G. Wang and L. Hu, *Adv. Energy Mater.*, 2021, **11**, 2002887.
64 G. Binitha, M. S. Soumya, A. A. Madhavan, P. Praveen, A. Balakrishnan, K. R. V. Subramanian, M. V. Reddy, S. V. Nair, A. S. Nair and N. Sivakumar, *J. Mater. Chem. A*, 2013, **1**, 11698.
65 A. Senthamizhan, B. Balusamy, Z. Aytac and T. Uyar, *CrystEngComm*, 2016, **18**, 6341.
66 Y. Li, H. Zhang, X. Zhang, L. Wei, Y. Zhang, G. Hai and Y. Sun, *J. Mater. Sci.: Mater. Electron.*, 2019, **30**, 15734.
67 D. Hu, R. Wang, P. Du, G. Li, Y. Wang, D. Fan and X. Pan, *Ceram. Int.*, 2022, **48**, 6549.
68 M. S. Kolathodi, M. Palei and T. S. Natarajan, *J. Mater. Chem. A*, 2015, **3**, 7513.
69 S. Santangelo, M. H. Raza, N. Pinna and S. Patanè, *Appl. Phys. Lett.*, 2021, **118**, 251105.
70 C. Triolo, S. Santangelo, B. Petrovičovà, M. G. Musolino, I. Rincón, A. Atxirika, S. Gil and Y. Belaustegui, *Appl. Sci.*, 2023, **13**, 721.
71 A. Mao, H. Z. Xiang, Z. G. Zhang, K. Kuramoto, H. Zhang and Y. Jia, *J. Magn. Magn. Mater.*, 2020, **497**, 165884.
72 F. Mou, J. G. Guan, W. Shi, Z. Sun and S. Wang, *Langmuir*, 2010, **26**, 15580.
73 J. Dąbrowa, M. Stygar, A. Mikuła, A. Knapik, K. Mroczka, W. Tejchman, M. Danielewski and M. Martin, *Mater. Lett.*, 2018, **216**, 32.
74 A. Mao, F. Quan, H. Z. Xiang, Z. G. Zhang, K. Kuramoto and A. L. Xia, *J. Mol. Struct.*, 2019, **1194**, 11.
75 D. Wang, S. Jiang, C. Duan, J. Mao, Y. Dong, K. Dong, Z. Wang, S. Luo, Y. Liu and X. Qi, *J. Alloys Compd.*, 2020, **844**, 156158.
76 B. Liang, Y. Ai, Y. Wang, C. Liu, S. Ouyang and M. Liu, *Materials*, 2020, **13**, 5798.
77 B. Talluri, K. Yoo and J. Kim, *J. Environ. Chem. Eng.*, 2022, **10**, 106932.
78 A. L. Patterson, *Phys. Rev.*, 1939, **56**, 978.
79 H. D. Lutz, B. Müller and H. J. Steiner, *J. Solid State Chem.*, 1991, **90**, 54.
80 P. Choudhary and D. Varshney, *Mater. Res. Express*, 2017, **4**, 076110.
81 B. Nandan, M. C. Bhatnagar and S. C. Kashyap, *J. Phys. Chem. Solids*, 2019, **129**, 298.
82 M. Foerster, M. Iliev, N. Dix, X. Martí, M. Barchuk, F. Sánchez and J. Fontcuberta, *Adv. Funct. Mater.*, 2012, **22**, 4344.
83 R. Chen, W. Wang, X. Zhao, Y. Zhang, S. Wu and F. Li, *Chem. Eng. J.*, 2014, **242**, 226.
84 W. Wang, Z. Ding, X. Zhao, S. Wu, F. Li, M. Yue and J. P. Liu, *J. Appl. Phys.*, 2015, **117**, 17A328.
85 G. Wang, J. Qin, Y. Feng, B. Feng, S. Yang, Z. Wang, Y. Zhao and J. Wei, high-entropy oxides, *ACS Appl. Mater. Interfaces*, 2020, **12**, 45155.
86 T. X. Nguyen, J. Patra, J. K. Chang and J. M. Ting, *J. Mater. Chem. A*, 2020, **8**, 18963.
87 G. C. Allen, S. J. Harris, J. A. Jutson and J. M. Dyke, *Appl. Surf. Sci.*, 1989, **37**, 111.
88 J. F. Moulder, W. F. Stickle, P. E. Sobol and K. D. Bomben, *Handbook of X-ray Photoelectron Spectroscopy: A Reference Book of Standard Spectra for Identification and Interpretation of XPS Data*, Physical Electronics Division, PerkinElmer Corporation, Eden Prairie, 55344 – Minnesota, USA, 1992.
89 A. Sarkar, B. Eggert, R. Witte, J. Lill, L. Velasco, Q. Wang, J. Sonar, K. Ollefs, S. S. Bhattacharya, R. A. Brand, H. Wende, F. M. F. de Grot, O. Clemens, H. Hahn and R. Kruk, *Acta Mater.*, 2022, **226**, 117581.
90 V. M. Jiménez, A. Fernández, J. P. Espinós and A. R. González-Elipe, *J. Electron Spectrosc. Relat. Phenom.*, 1995, **71**, 61.
91 F. A. Bushira, P. Wang and Y. Jin, *Anal. Chem.*, 2022, **94**, 2958.
92 J. Bao, X. Zhang, B. Fan, J. Zhang, M. Zhou, W. Yang, X. Hu, H. Wang, B. Pan and Y. Xie, *Angew. Chem., Int. Ed.*, 2015, **54**, 7399.
93 J. H. Kim, Y. J. Jang, J. H. Kim, J. W. Jang, S. H. Choi and J. S. Lee, *Nanoscale*, 2015, **7**, 19144.

94 T. Dickinson, A. F. Povey and P. M. A. Sherwood, *J. Chem. Soc., Faraday Trans. 1*, 1976, **72**, 686.
95 V. Nefedov, D. Gati, B. Dzhurinskii, N. Sergushin and Y. V. Salyn, X-ray electron study of oxides of elements, *Zh. Neorg. Khim.*, 1975, **20**, 2307.
96 C. D. Wagner, D. A. Zatko and R. H. Raymond, *Anal. Chem.*, 1980, **52**, 1445.
97 S. Jiang, K. Tian, X. Li, C. Duan, D. Wang, Z. Wang, H. Sun, R. Zheng and Y. Liu, *J. Colloid Interface Sci.*, 2022, **606**, 635.
98 L. Li, G. Li, Y. Zhang, W. Ouyang, H. Zhang, F. Dong, X. Gao and Z. Lin, *J. Mater. Chem. A*, 2020, **8**, 25687.
99 R. D. Shannon, *Acta Crystallogr., Sect. A: Cryst. Phys., Diffr., Theor. Gen. Crystallogr.*, 1976, **32**, 751.
100 R. Farhat, J. Dhainy and L. I. Halaoui, *ACS Catal.*, 2019, **10**, 20.